Original scientific paper
https://doi.org/10.33180/InfMIDEM2022.103

Informacije MIDEM
Journal of Microelectronics,
Electronic Components and Materials
Vol. 52, No. 1(2022), 17 – 27

Operation of Permanent Magnet Synchronous Motor after Open-circuit Battery Supply Fault

Vanja Ambrožič[1], Mitja Breznik[2], Mitja Nemec[1]

[1]University of Ljubljana, Faculty of Electrical Engineering, Ljubljana, Slovenia
[2]Kolektor Group d.o.o., Idrija, Slovenia

Abstract: This paper presents a method for post-fault operation with reduced performance of a permanent magnet synchronous motor following a battery supply open circuit fault. The approach upgrades the previously developed fast model-oriented supply fault detection algorithm based on comparing actual and estimated values of a DC-link voltage. The latter is determined by the model of supply circuit and observer of battery open-circuit voltage. Implementing a post-fault concept does not require additional hardware, as it uses quantities from an already existent vector control algorithm. After the fault is detected, the algorithm is upgraded by a DC-link voltage cascade control loop. An analytical approach to parametrization of the controller, based on the linearization and the reduction of the system's transfer function, is also proposed. Simulations and experimental results have validated the performance of the post-fault algorithm.

Keywords: power supply fault; model-based detection algorithm; control loop parametrization; DC-link voltage regulator; fault-tolerant design

Delovanje sinhronskega motorja s trajnimi magneti po izpadu akumulatorskega napajanja

Izvleček: Članek predstavi metodo za nadaljevanje obratovanja sinhronskega stroja s trajnimi magneti z zmanjšano zmogljivostjo po izpadu akumulatorskega napajanja. Pristop nadgrajuje že razviti modelsko orientirani algoritem za ugotavljanje izpada napajanja, ki sloni na primerjavi dejanske in ocenjene vrednosti napetosti vmesnega tokokroga. Slednjo ugotavljamo prek modela napajalnega vezja in opazovalnika napetosti odprtih sponk akumulatorja. Implementacija koncepta obratovanja stroja po napaki ne zahteva dodatne aparaturne nadgradnje, ker uporablja že obstoječe količine, potrebne za normalno delovanje. Regulacijski algoritem po detekciji napake nadgradimo s kaskadno zanko za regulacijo napetosti vmesnega tokokroga. V članku je predstavljeno tudi analitično parametriziranje regulatorja, ki sloni na linearizaciji in redukciji sistemske prenosne funkcije. Simulacije in eksperimentalni rezultati potrjujejo učinkovitost obratovanja po napaki.

Ključne besede: izpad napajanja, modelno zasnovani detekcijski algoritem, parametriziranje regulacijske zanke, regulator napetosti vmesnega tokokroga, zasnova odporna na izpade

** Corresponding Author's e-mail: vanja.ambrozic@fe.uni-lj.si*

1 Introduction

Battery-supplied permanent magnet synchronous motor (PMSM) often appears as the main or auxiliary component in various mobility applications due to its high efficiency and high power density [1]. Therefore, research on fault mechanisms and post-fault operation of systems that enable key operational features in a vehicle is the basis for providing appropriate safety and reliability. The probability of a supply system failure has already been extensively investigated [2]. However, the development of diagnostic and post-fault operation methods for a drive in case of power supply failure

How to cite:
V. Ambrožič et al., "Operation of Permanent Magnet Synchronous Motor after Open-circuit Battery Supply Fault", Inf. Midem-J. Microelectron. Electron. Compon. Mater., Vol. 52, No. 1(2022), pp. 17–27

lags behind the successfully implemented solutions that cope with the faults in PMSM, converter, and/or appropriate sensors [3]–[10]

The interruption of the supply system can be caused by damage or change of operational state (e.g., disconnection due to safe stop) of individual drive subsystems. One of these is an intermediate DC/DC converter whose failure may prevent the proper energy flow. Method for fault detection of switching elements in a step-down converter feeding a brushless DC machine is proposed in [11]. Different fault scenarios in a parallel DC/DC converter for interconnecting electrical drive and various power sources are analyzed in [12].

The fault mechanism and consequent detection methods for battery voltage sources have been thoroughly investigated. The number of connections between individual battery cells increases the fault probability, which is reflected through galvanic interruptions, an increase of impedance, or a decrease in power capacity. The fault/breakage detection of welds between battery cells in electric vehicles, based on a statistical energy capacity determination, has been investigated in [13]. A comprehensive overview of supply systems fault diagnosis based on Li-Ion technology has been presented in [14].

A high-voltage battery system in hybrid and electric vehicles is connected to the rest of the drive through a contactor. The interruption of the contactor, with subsequent disconnection of a supply circuit, is implemented in case of a safe stop or emergency shutdown following an accident. In case of an emergency shutdown, a safe level of DC-link voltage has to be provided in conformity with ECE R94 [15]. A method for reducing the voltage without a braking resistor has been presented in [16]. Operation is based on upgrading the field-oriented control (FOC) with a DC-link voltage controller and modulation index controller. The detection method and guidelines for the determination of controller parameters are not presented.

Supervision of the energy flow and DC-link voltage level is crucial in drives with diode rectifiers. Dynamic braking of the PMSM can be achieved by directing the mechanical energy into additional Joule losses in the machine's windings. The DC-link voltage level is limited by keeping machine losses equal to braking power through stator current *d* and *q* components in the field reference frame [17]. Control algorithm for braking of switched reluctance machine is also proposed [18]. Limited braking capability and consequent regenerative performance are also present in battery-fed electrical drives that are close to energy capacity limits. In [19], the approach for limiting the energy flow into the DC supply through the increase of losses by injecting high-frequency current components into the *d* axis of an induction motor is presented.

Operating conditions, similar to those caused by the fault of the supply system, can be found in FOC doubly-fed induction generators in island operation [20]. The system provides for the DC load voltage and supplies the rotor windings with AC voltage oscillating at slip frequency. A separate control loop controls DC-link voltage, adapting it to the reference. A cascade voltage control of a three-phase rectifier DC-link voltage has been studied in [21]. The output power of the load is determined by the observer that allows for the implementation of the inner control loop based on the power reference.

Finally, it can be concluded that due to the complexity of supply systems, several sources and causes can interrupt the energy flow. If the PMSM drive operates in the regenerative mode or the field weakening region, this fault may produce secondary damage caused by the failure of electronic components due to overvoltage [9].

In this paper, a detection method and appropriate control algorithm that prevents secondary damage without the need for additional hardware modifications (e.g., braking resistors, electronic components with higher values of the maximum permitted voltages) is presented. In order to ensure a fast and robust transition to the post-fault operation, a model-oriented algorithm for real-time detection of supply interruption has been applied. As a result, the diagnostic method and post-fault algorithm constitute a fault-tolerant system, based on the most commonly used configuration of the supply system and control method for PMSM (FOC).

Post-fault control approach and analytical guidelines for controllers' parametrization provide for:

- maintaining the DC-link voltage level inside predetermined operational boundaries. The maximum voltage is defined by the maximum permitted voltage of the converter's electronic components. On the other side, the minimum voltage level is defined by the minimum supply voltage required by the converter's peripheral and logic units in the case of controllers with a single supply.
- control of PMSM electrical quantities, even in field weakening region.
- potential for upgrading the control scheme that enables the drive's deceleration by injecting the currents that cause additional losses in the system.
- sufficient time for the electronics to enter the safe-stop mode.

2 System definition

The proposed method is developed for a standard and straightforward system of battery-fed PMSM drive. The system consists of Li-Ion batteries, supply cables, inverter with accompanying capacitor bank, and a PMSM. Block scheme of individual parts of the drive with potential failure locations is depicted in Fig. 1. Although this paper presents a method designed for a specific configuration, the approach could be easily adapted to different types of machines and topologies of supply circuits, since it is based on modelling of the supply circuit and well-established control principle.

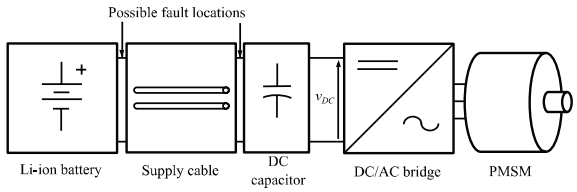

Figure 1: Graphic representation of the analyzed system.

Block scheme showing FOC of PMSM drive, capable of operating in field weakening region, is shown in Fig. 2 [22]. The scheme already includes proposed fault detection and a post-fault approach (inside a dotted rectangle), described in detail in the following sections. The symmetrical voltage model of PMSM in *d-q* rotor field coordinates is determined by (1), where v_d, v_q, i_d and i_q represent stator voltages and currents in a rotor reference frame. R_s, L_d, L_q and ψ_m denote stator resistance, inductances, and flux of the rotor's permanent magnet, respectively. Electromagnetic torque T_e in case of surface-mounted permanent magnet motor (SPM) or interior permanent magnet motor (IPM) with similar L_d and L_q can be defined by (2), where p_p is the number of pole pairs. Electric power is defined by (3).

$$\begin{bmatrix} v_d \\ v_q \end{bmatrix} = \begin{bmatrix} R_s + sL_d & -\omega L_q \\ \omega L_d & R_s + sL_q \end{bmatrix} \begin{bmatrix} i_d \\ i_q \end{bmatrix} + \begin{bmatrix} 0 \\ \omega \psi_m \end{bmatrix} \tag{1}$$

$$T_e = \frac{3}{2} p_p i_q \psi_m \tag{2}$$

$$p_e = \frac{3}{2} p_p (v_d i_d + v_q i_q) \tag{3}$$

3 Fault detection

The dynamics of post-fault response depends on fast and reliable fault detection to avoid false positives or false negatives. In this paper, the post-fault algorithm relies on the model-based detection that has been proven effective [23]. Possible open-circuit fault locations depicted in Fig. 1 can be quickly detected by monitoring the change of DC-link voltage. However, only a specific change to this phenomenon must be considered, while the changes due to regular operation should be ignored. This task can be achieved by comparing the measured DC-link voltage (measurement performed in almost every drive) to the one obtained through the model.

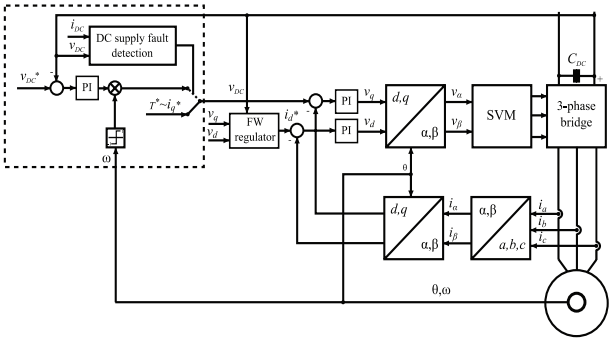

Figure 2: The control scheme of PMSM drive with added detection and post-fault control blocks.

Furthermore, the model and corresponding control circuit must be robust and self-adaptable to slow changes. These are caused by battery state-of-charge and parasitic effects, which occur during regular operation and react only to fast changes, owing to an open circuit. The model is based on a Thévenin's circuit shown in Fig. 3, where i_{batt} and v_{batt} denote battery current and voltage, i_{DC} and v_{DC} are DC-link current and voltage. v_{oc} is the battery's open-circuit voltage, and R_i is its internal resistance. Supply cable is represented by resistance R_c and inductance L_c of the transmission path, as calculated from [24]. Total capacitance C_{DC} and series resistance R_{esr} represent DC-link capacitor bank.

Since linear elements form the electrical circuit, the model estimated DC-link voltage ($\hat{v}_{DC}$) could be calculated as the sum of two terms that depend on i_{DC} and v_{oc}, respectively

$$\hat{v}_{DC} = \hat{v}_{DC}^{i_{DC}} + \hat{v}_{DC}^{v_{oc}} \tag{4}$$

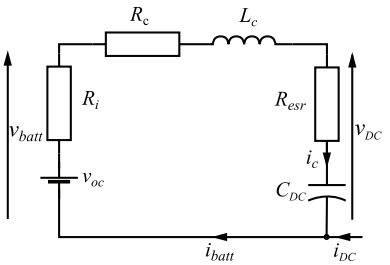

Figure 3: Lumped element electric circuit model of DC supply.

The transfer functions of the two terms are defined as

$$F_{iDC}(s)=\frac{\hat{v}_{DC}^{i_{DC}}(s)}{i_{DC}(s)}= \\ =\frac{R_i+R_c+sC_{DC}R_{esr}\left(R_c+R_i\right)+sL_c+s^2L_cC_{DC}R_{esr}}{-1-sC_{DC}\left(R_i+R_c+R_{esr}\right)-s^2L_cC_{DC}} \quad (5)$$

and

$$F_{voc}(s)=\frac{\hat{v}_{DC}^{v_{oc}}(s)}{\hat{v}_{oc}(s)}= \\ =\frac{1+sC_{DC}R_{esr}}{1+sC_{DC}\left(R_{esr}+R_i+R_c\right)+s^2L_cC_{DC}} \quad (6)$$

as represented in a block scheme in Fig. 4.

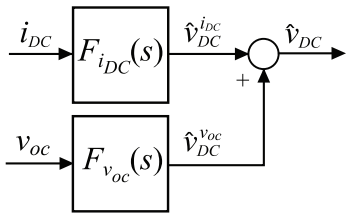

Figure 4: Block diagram of a DC supply model.

As previously mentioned, the main idea of the diagnostic approach to battery open circuit detection is to monitor the difference between the estimated and measured v_{DC} (Fig. 5). Consequently, in an open circuit, the measured and the estimated value will differ. However, the erroneous estimation may also generate the difference, thus leading to a false positive. The causes for this effect are either altered battery voltage (v_{oc}) or erroneously estimated/modified lumped circuit parameters.

The change of battery open circuit voltage v_{oc} during operation is normal and relatively slow. Thus its estimation should be incorporated into the diagnostic scheme (Fig. 5) that now has to fulfill two tasks:

- $\hat{v}_{oc}$ estimation: $\hat{v}_{oc}$ is needed for $\hat{v}_{DC}$ estimation in (4) and (6). Fortunately, during normal operation $\hat{v}_{oc}$, and consequently the v_{DC} estimation error *e*, change slowly; thus the slower and stable inner control algorithm should adapt the estimated value $\hat{v}_{oc}$ and so minimize the error. A possible solution could be using the sliding mode observer [23,25].
- Battery open-circuit fault detection: Sudden error between measured and estimated DC-link voltage *e*, after $\hat{v}_{oc}$ has been adequately tracked, could be caused only by some other fault source – open circuit – as will be explained next.

At steady-state (5) and (6) can be simplified, leading to the equation for DC link voltage error from Fig. 5

$$\varepsilon_m=\underbrace{v_{DC}-\hat{v}_{DC}}_{\varepsilon}\pm\zeta_\varepsilon=\underbrace{v_{DC}-\hat{v}_{oc}+i_{DC}\left(R_i+R_C\right)}_{\varepsilon}\pm\zeta_\varepsilon= \\ v_{DC}-\hat{v}_{oc}+\frac{3}{2v_{DC}}\left(v_di_d-v_qi_q\right)\left(R_i+R_C\right)\pm\zeta_\varepsilon \quad (7)$$

The term consists of:

- ε – the difference between measured (v_{DC}) and estimated ($\hat{v}_{DC}$) DC-link voltage. Note that i_{DC} in $\hat{v}_{DC}$ is calculated from control variables instead of being measured.
- ζ_e – the error due to erroneous modeling (parameter mismatch, discretization, measurement error, etc.)

The maximum possible error of ζ_e (denoted as ζ_{e_max}) can be analytically determined and serves as a diagnostic threshold. Hence, as depicted in Fig. 5, if the error ε_m exceeds $\zeta_e = \zeta_{e\_max}$, the open circuit has undoubtedly occurred.

Such diagnostic method proves to be reliable and fast, allowing for fast post-fault operation.

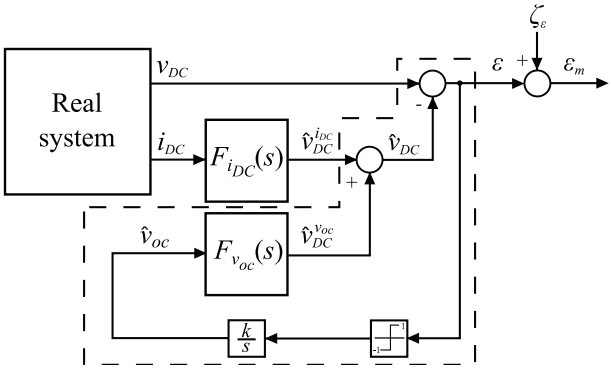

Figure 5: Block diagram of the estimation model.

4 Post fault operation

Once the fault is detected, post fault operation can be performed in two ways. The first one is to shut down the inverter. While the simplest to implement, this option is only viable when the drive is not in a field weakening mode or the inverter's DC link does not supply the electronics. During field weakening, current control has to stay active. Also, if the inverter's DC link should supply the electronics, rotational energy can be used to provide the necessary power, at least for some time.

The DClink voltage can change significantly during the fault transient, as the magnetic energy stored in machine windings dissipates to the DC-link regardless of

the post fault operation mode. Therefore, for the inverter to survive such a fault, it has to be designed accordingly. Only then can the inverter take appropriate action to control the DC-link voltage.

4.1 Inverter design considerations for open circuit battery supply fault

Immediately following the fault, i_d should remain unchanged. It is already zero in a constant torque mode, while in field weakening mode, it prevents back emf from rising above a safe level. The only active required power flow is for supplying the control electronics and the motor losses. Hence, the active power current component i_q after the fault transient will be almost zero.

After the fault, the energy circulates only between the machine and the inverter. After inserting (1) into (3), three distinct power flow components can be identified: winding losses (P_{loss}), reactive power (P_r), and mechanical power (P_{mech}) (8).

$$p_e = \frac{3}{2}\left(\underbrace{R_s i_d^{\,2} + R_s i_q^{\,2}}_{P_{loss}} + \underbrace{L_d i_d \frac{di_d}{dt} + L_q i_q \frac{di_q}{dt}}_{P_r} + \underbrace{\omega \psi_m i_q + \omega i_d i_q (L_d - L_q)}_{P_{mech}} \right) \tag{8}$$

In order to assess the under-/overvoltage, the energy transferred from fault occurrence until the end of fault transient (t_1) should be calculated .

$$\Delta W = \int_0^{t_1} p_e dt = \frac{3}{2}\int_0^{t_1} \left(R_s \left(i_d^{\,2} + i_q^{\,2} \right) + \omega i_q \left(\psi_m + i_d (L_d - L_q) \right) \right) dt - \frac{3 L_q i_{q0}^2}{4} \tag{9}$$

The amount of transferred magnetic (reactive) energy does not depend on the transient duration but only on the current values at the beginning of the transient i_{d0}, i_{q0} ($t=0$). Additionally, since i_d remains almost unaltered, its derivative can be neglected.

The total duration of the fault transient (t_1) consists of fault detection time t_{det} and current transient time $\mathrm{D}t$ (assuming local linearity, see (13))

$$t_1 = t_{det} + \Delta t \tag{10}$$

The final equation for the total energy transferred during the transient is

$$\Delta W = \frac{3}{2}\left((R_s i_{q0}^2 + \omega \psi_m i_{q0})(t_{det} + \frac{\Delta t}{2}) - L_q \frac{i_{q0}^2}{2} \right) \tag{11}$$

With a shorter total time t_1, the energy transferred between the machine and inverter will be lower; thus, the under-/overvoltage on DC-link will be reduced.

The main parameters determining the duration of the current transient (Δt) are machine inductances L_d, L_q, and the voltage difference between maximum applicable inverter voltage and back emf.

$$\sqrt{v_d^2 + v_q^2} = \frac{v_{DC}}{\sqrt{3}} \tag{12}$$

Insertion of (1) into (12), neglecting the terms with resistance R_s (being significantly smaller than other contributions) and di_d/dt (since i_d remains constant), and also assuming linear transition of i_q ($di_q/dt = -i_{q0}/\Delta t$) results in .

$$(L_q \frac{-i_{q0}}{\Delta t} + \omega L_d i_{d0} + \omega \psi_m)^2 = \frac{v_{DC}^2}{3} - (-\omega L_q i_{q0})^2 \tag{13}$$

The solutions of the quadratic equation for Δt with different i_d, i_q pairs in $i_d < 0$ half-plane (which corresponds to normal operation/field weakening), show that the transient time $\mathrm{D}t$ mainly depends on i_q (Fig 6).

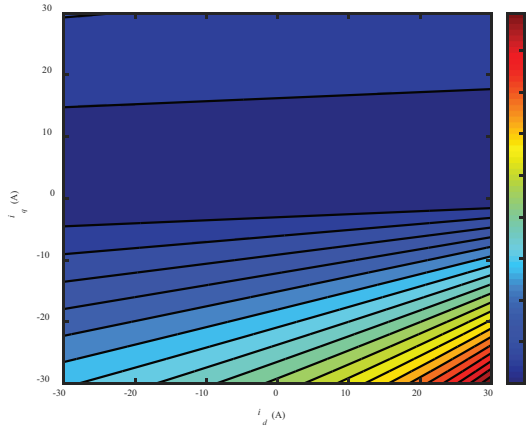

Figure 6: Transient duration.

The total energy transferred will alter the energy level in the DC-link capacitor (14), resulting in either an increased or decreased DC voltage (v_{DC_1}) compared to the voltage at the instant of the fault v_{DC_0}. Using (11) and (14), the relation between final DC-link voltage v_{DC_1} and DC-link capacitance is obtained (15).

$$\Delta W = \frac{C_{DC}(v_{DC\_1}^2 - v_{DC\_0}^2)}{2} \tag{14}$$

$$v_{DC\_1} = \sqrt{v_{DC\_0}^2 - \frac{3}{C_{DC}^2}\alpha} \tag{15}$$

where

$$\alpha = \left(R_s i_{q0}^2 + \omega \psi_m i_{q0}\right)\left(t_{det} + \frac{\Delta t}{2}\right) - \frac{L_q i_{q0}^2}{2}$$

Equation (15) serves as a design criterion for assessing the drive's tolerance during the supply fault to overvoltage, when in generator mode, and undervoltage, in motoring mode.

4.2 Post-fault DC-link voltage control

After the supply fault detection, the DC link voltage has to stay under control, especially in field weakening mode, to prevent further faults. Since the field weakening controller still sets the direct current id in this case, the voltage can be controlled by quadrature current i_q. The sign of i_q has to account for the direction of rotation (dotted area in Fig. 2).

4.2.1 Tuning DC-link voltage controller

The selection of voltage controller parameters is especially critical for achieving fast transients. In order to set the parameters analytically, the control loop (Fig. 7) has to be analyzed.

Electric power drawn from the DC-link depends on the speed and torque of the machine, with losses in machine and inverter neglected (16).

$$p_e = T_e \frac{\omega}{p_p} = \frac{3}{2}\omega i_q \psi_m \tag{16}$$

Thus, the DC-link voltage is

$$v_{DC} = i_{DC} R_{esr} + \frac{1}{sC_{DC}} i_{DC} \tag{17}$$

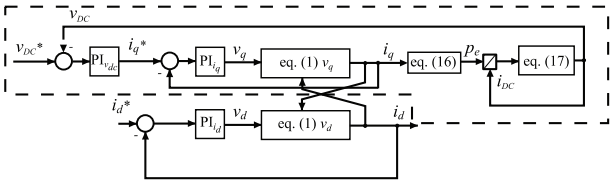

Figure 7: Block scheme of a post-fault voltage control loop.

As can be seen, the control loop is nonlinear and depends on multiple input parameters. However, several simplifications can be introduced to obtain an analytically solvable system.

Nonlinear relationship in DC-link current i_{DC} calculation from power p_e can be linearized as the loop will operate only around the DC-link voltage reference value. Hence DC link voltage (v_{DC}) can be considered pseudo-constant resulting in the division (far right-hand side on Fig. 7) being replaced by multiplication with constant v_{DC}^{-1}.

Furthermore, as the mechanical speed ω dynamics is several orders of magnitude slower than electrical transients, the mechanical speed can also be considered constant during these transients. Consequently, the direct axes current i_d, which is used only for field weakening (the latter is a function of ω), can also be considered constant. Hence, the i_d control loop in Fig. 7 is oblivious.

Thus the transfer function of the system, including i_q current PI controller with gains K_{p_q}, K_{i_q} (dashed in Fig. 6), is

$$F_s = \frac{3}{2}\frac{\omega \psi_m}{v_{DC}^* C_{DC}} \cdot \frac{K_{p\_q} C_{DC} R_{esr} s^2 + (K_{p\_q} + K_{i\_q} C_{DC} R_{esr}) s + K_{i\_q}}{L_q s^3 + (K_{p\_q} + R_s) s^2 + K_{i\_q} s} \tag{18}$$

The equation can be rewritten in a form where individual time constants can be easily identified

$$F_s = \frac{3}{2}\omega \psi_m \frac{K_{i\_q}\tau_1\tau_2}{v_{DC}^* C_{DC} L_q} \frac{\left(\frac{K_{p\_q}}{K_{i\_q}} s + 1\right)(C_{DC} R_{esr} s + 1)}{s(\tau_1 s + 1)(\tau_2 s + 1)} \tag{19}$$

where

$$\tau_{1,2} = \frac{2L_q}{K_{p\_q} + R_s \pm \sqrt{\left(K_{p\_q} + R_s\right)^2 - 4L_q K_{i\_q}}} \tag{20}$$

By setting the current controller parameters $K_{p\_q}/K_{i\_q} = \tau_2$, the order of the transfer function is further reduced [26,27]. Additional simplification is possible by neglecting R_{esr}. The result of this reduction is a second-order system (21).

$$F_s = \frac{3}{2}\omega \psi_m \frac{\tau_1 K_{p\_q}}{v_{DC}^* C_{DC} L_q} \frac{1}{s(\tau_1 s + 1)} \tag{21}$$

This system can be further reduced to an integrator with a delay (22).

$$F_s(s) = k' \frac{e^{-\tau_d s}}{s} \tag{22}$$

with gain defined as

$$k' = \frac{3}{2}\omega\psi_m \frac{\tau_1 K_{p\_q}}{v_{DC}{}^* C_{DC} L_q} \quad (23)$$

The delay τ_d is calculated as proposed in [27]

$$\tau_d = \frac{\tau_1}{2} + \frac{\tau_s}{2} \quad (24)$$

using a time constant of the initial transfer function $_1$, and sampling time τ_s.

Now a voltage PI controller can be parametrized. "Simple control" or "Skogestad (SIMC)" guidelines offer the recipe for setting the (voltage) controller parameters for the transfer function in form equal to (25), where $_c$ is the desired closed loop time constant.

$$k_p = \frac{1}{k'} \frac{1}{(\tau_c + \theta)}, \tau_i = 4(\tau_c + \theta) \quad (25)$$

The v_{DC} control should function regardless of the operational point. As the system gain k' actually depends on rotor speed and DC voltage reference setpoint (23), the proportional k_p gain in (25) has to adapt accordingly.

5 Simulation results

First, the simulations were performed to test if the simplifications of the DC-link voltage control loop in section 4 were justified. The parameters correspond to those of the experimental system (Tables 1 and 2).

The transient response of a simplified system based on (18) and fully nonlinear system described in (8), were compared. The controller parameters for both systems were set using (25). As shown in Fig. 8 and 9, the only significant difference between the two systems occurs during the initial transient of the DC-link voltage. As the voltage controller response is much slower, the transient error owed to the simplification has no effect. The agreement between the responses of both models during the main transient shows that the simplifications were justified and that the voltage controller was correctly parameterized.

Additionally, the enlarged transient of i_q in Fig. 9 corroborates the duration of the transient obtained from (13).

6 Experimental results

6.1 Experimental setup

Detection algorithm and post-fault operation were tested on a laboratory back-to-back setup consisting of

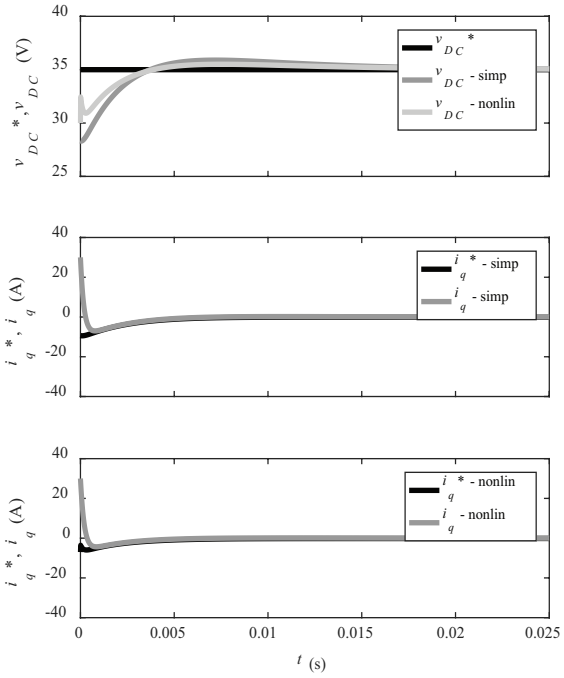

Figure 8: Transient response of simplified ("simp") and fully nonlinear ("nonlin") model in motoring mode.

two identical PMSM drives with independent battery power supplies, thus enabling four-quadrant operation (see Figs. 10-11). Control and detection algorithm (running at 6 kHz) was implemented on a motor controller build around ARM Cortex M4 MCU with support for floating-point arithmetic. The drive under test is

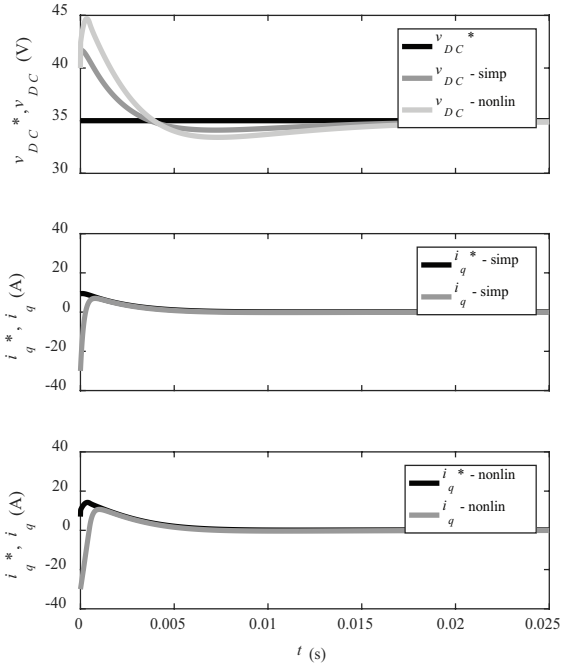

Figure 9: Transient response of simplified ("simp") and fully non-linear ("nonlin") model in generator mode.

torque-controlled, which is the usual operation mode in traction applications. A second coupled drive emulates the mechanical load by running at a controlled speed. Power electronics is integrated into both motors' housings. Fault emulation was performed by switching off the contactor of the torque controlled drive.

Inverter and power supply parameters are shown in Table 1, while the machine parameters are given in Table 2.

Table 1: DC Supply parameters

Symbol	Value	Unit
v_{oc}	34.5	(V)
R_i	86	(mΩ)
R_c	94	(mΩ)
L_c	3.82·10-6	(H)
r_c	0.6	(mm)
d_c	0.1	(m)
l_c	1.8	(m)
C_{DC}	1.4	(mF)
R_{esr}	94.1	(mΩ)
k_i	0.5	/

Table 2: PMSM parameters

Symbol	Value	Unit
R_s	28.5	(mΩ)
L_d	164	(mH)
L_q	186	(mH)
Ψ_m	0.022	(Wb)
p_p	4	/

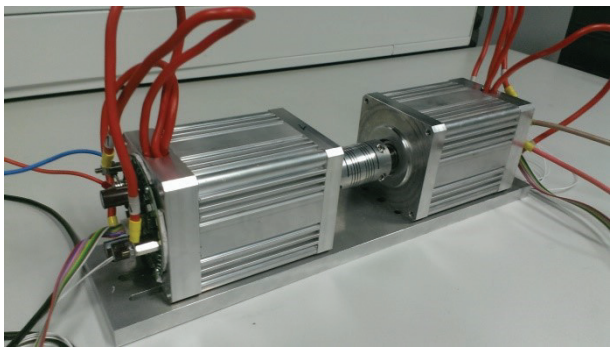

Figure 10: Experimental setup with back-to-back configuration.

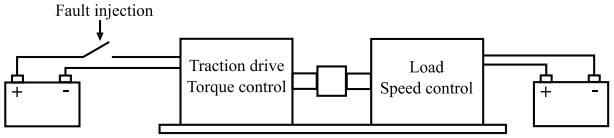

Figure 11: Schematic of the experimental setup.

6.2 Fault detection

Firstly, the performance of the DC-link voltage observer for fault detection, described in section 3, is shown under normal operation [23]. As we can see (fig. 12), the observer tracks the actual voltage during the drive's operating point changes without any significant deviations.

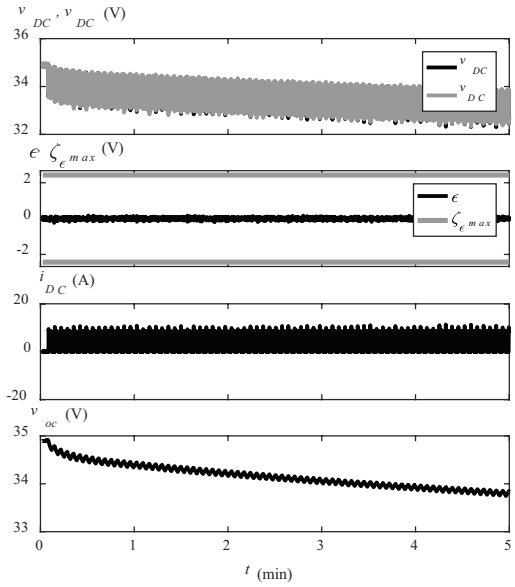

Figure 12: DC supply model response in case of periodic changes of drive's operating point.

The response of the fault detection algorithm during the fault in generator mode is shown in fig. 13. At the instant of the fault, the error between the actual DC-

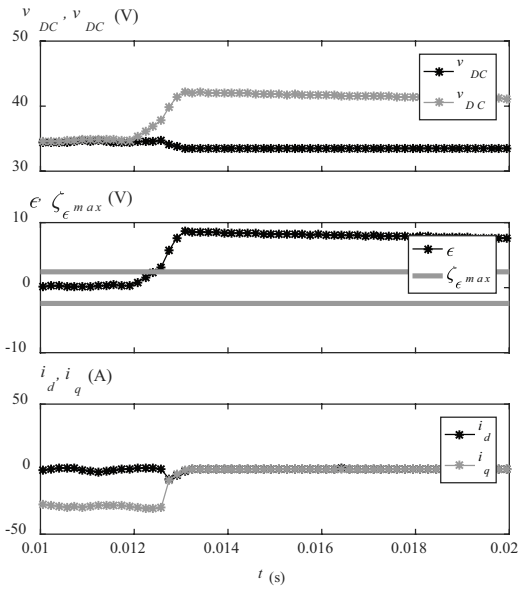

Figure 13: Transient response during a fault in generator mode without voltage controller (1500 rpm, i_q^* = - 30 A).

link voltage and observer output almost immediately exceeds the threshold resulting in instantaneous fault detection. Note that this test is only for demonstration purposes, as no pos-fault action is undertaken.

6.3 Post fault operation

Results in this section show the system response with both the fault detection and post-fault control method activated. A fast voltage control loop response can be observed, as the DC-link voltage stabilizes quickly to the reference value (Fig. 14-15) in both the motor and generator mode. In motor mode (Fig. 14), a short-lasting and minor undervoltage occurs. Hence, the drives with electronics supplied from the DC-link can continue to operate even after the fault. Even more important is the behavior in generator mode (Fig. 15). Here the voltage controller prevents more extended overvoltage, which would occur without a post-fault voltage controller (Fig. 13). Additionally, the overvoltage is very close to the theoretically calculated value from (15), where during generator operation, 46,8 V was measured. In comparison, 46,5 V was calculated from the analytical equation based on system parameters. The combined detection and activation time of four sampling intervals (three for fault detection and one for starting the post-fault mode) was considered for the analytical approach. This confirms the practicality of (15), when designing the drive, thus providing the basis for the maximum voltage ratings of electronic components.

Safe DC-link voltage level with a disconnected power supply can be provided only by the fading kinetic energy of the system's rotating parts. Its duration depends on the actual speed at the instant of the fault and the system's inertia. However, this time should be more than enough for the electronics to enter the safe-stop mode, including the storage of relevant parameters. Hence, almost all of the (kinetic) energy is supporting a low-consuming operation of the control electronics.

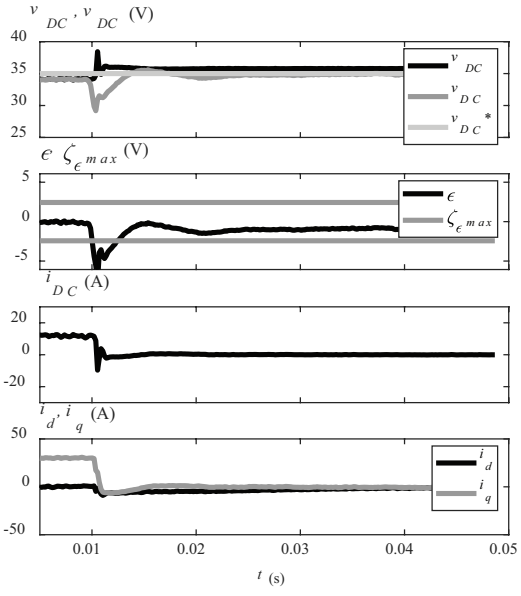

Figure 14: Transient response during a fault in motor mode (1500 rpm, i_q^* = 30 A).

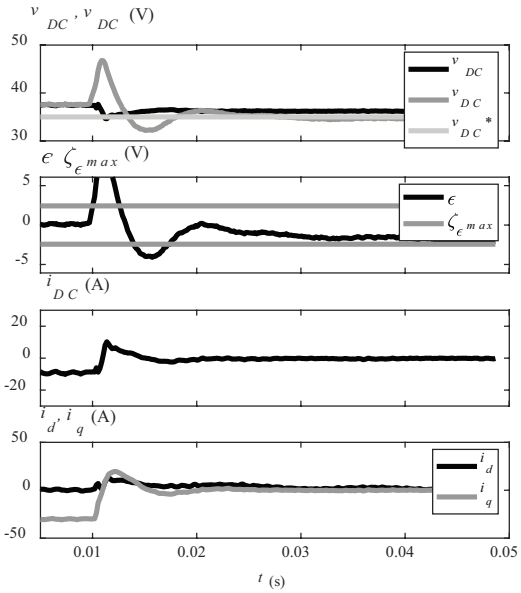

Figure 15: Transient response during fault in generator mode (1500 rpm, i_q^* = - 30 A).

7 Conclusion

This paper proposed an approach to post-fault operation following the malfunctioning of the battery power supply of a PMSM drive. The main goal is to control the level of DC-link voltage and provide for a temporary supply of the controller's electronics before entering the safe-stop mode. The functionality of a post-fault operation, following successful fault detection, has been confirmed by the simulation and experimental results. These also confirm the validity of the analytical terms to determine limit values of DC-link voltage during the transition to the post-fault operation. Further work will focus on applying the concept to more complex configurations of the supply system and methods for dynamic braking.

8 References

1. D. Cabezuelo, E. Ibarra, E. Planas, I. Kortabarria, and J. I. Garate, 'Rare-Earth Free EV and HEV Motor Drives: State of the Art', in *PCIM Europe 2018; International Exhibition and Conference for Power*

Electronics, Intelligent Motion, Renewable Energy and Energy Management, Jun. 2018, pp. 1–8.
2. D. Wanner, *Controlling over-actuated road vehicles during failure conditions*. Stockholm: Engineering Sciences, KTH Royal Institute of Technology, 2015. Accessed: Sep. 29, 2018. [Online]. Available: http://urn.kb.se/resolve?urn=urn:nbn:se:kth:diva-166819
3. J. Zheng, Z. Wang, D. Wang, Y. Li, and M. Li, 'Review of fault diagnosis of PMSM drive system in electric vehicles', in *2017 36th Chinese Control Conference (CCC)*, Jul. 2017, pp. 7426–7432. https://doi.org/10.23919/ChiCC.2017.8028529.
4. Y. Da, X. Shi, and M. Krishnamurthy, 'Health monitoring, fault diagnosis and failure prognosis techniques for Brushless Permanent Magnet Machines', in *2011 IEEE Vehicle Power and Propulsion Conference*, Sep. 2011, pp. 1–7. https://doi.org/10.1109/VPPC.2011.6043248.
5. A. M. El-Refaie, 'Fault-tolerant permanent magnet machines: a review', *IET Electr. Power Appl.*, vol. 5, no. 1, pp. 59–74, Jan. 2011, https://doi.org/10.1049/iet-epa.2009.0117.
6. T. A. Najafabadi, F. R. Salmasi, and P. Jabehdar-Maralani, 'Detection and Isolation of Speed-, DC-Link Voltage-, and Current-Sensor Faults Based on an Adaptive Observer in Induction-Motor Drives', *IEEE Trans. Ind. Electron.*, vol. 58, no. 5, pp. 1662–1672, May 2011, https://doi.org/10.1109/TIE.2010.2055775.
7. J. O. Estima, N. M. A. Freire, and A. J. M. Cardoso, 'Recent advances in fault diagnosis by Park's vector approach', in *2013 IEEE Workshop on Electrical Machines Design, Control and Diagnosis (WEMDCD)*, Mar. 2013, pp. 279–288. https://doi.org10.1109/WEMDCD.2013.6525187.
8. W. Zhang, D. Xu, P. N. Enjeti, H. Li, J. T. Hawke, and H. S. Krishnamoorthy, 'Survey on Fault-Tolerant Techniques for Power Electronic Converters', *IEEE Trans. Power Electron.*, vol. 29, no. 12, pp. 6319–6331, Dec. 2014, https://doi.org/10.1109/TPEL.2014.2304561.
9. L. Mathe, C. Kopacz, L. Bede, and P. O. Rasmussen, 'Sensor-fault tolerant control of PMSM in flux-weakening operation using LKF observer', in *Railway and Ship Propulsion 2012 Electrical Systems for Aircraft*, Oct. 2012, pp. 1–6. https://doi.org/10.1109/ESARS.2012.6387427.
10. S. K. E. Khil, I. Jlassi, J. O. Estima, N. Mrabet-Bellaaj, and A. J. M. Cardoso, 'Detection and isolation of open-switch and current sensor faults in PMSM drives, through stator current analysis', in *2017 IEEE 11th International Symposium on Diagnostics for Electrical Machines, Power Electronics and Drives (SDEMPED)*, Aug. 2017, pp. 373–379. https://doi.org/10.1109/DEMPED.2017.8062382.
11. J. Fang, W. Li, H. Li, and X. Xu, 'Online Inverter Fault Diagnosis of Buck-Converter BLDC Motor Combinations', *IEEE Trans. Power Electron.*, vol. 30, no. 5, pp. 2674–2688, May 2015, https://doi.org/10.1109/TPEL.2014.2330420.
12. H. Al-Sheikh, O. Bennouna, G. Hoblos, and N. Moubayed, 'Modeling, design and fault analysis of bidirectional DC-DC converter for hybrid electric vehicles', in *2014 IEEE 23rd International Symposium on Industrial Electronics (ISIE)*, Jun. 2014, pp. 1689–1695. https://doi.org/10.1109/ISIE.2014.6864869.
13. Y. Cai, L. Lu, P. Shen, X. Feng, H. Wang, and M. Ouyang, 'Online Weld Breakage Diagnosis for the Battery of Electric Vehicle: A Data-Driven Approach', in *2016 IEEE Vehicle Power and Propulsion Conference (VPPC)*, Oct. 2016, pp. 1–5. https://doi.org/10.1109/VPPC.2016.7791739.
14. C. Wu, C. Zhu, Y. Ge, and Y. Zhao, 'A review on fault mechanism and diagnosis approach for Li-ion batteries', *J. Nanomater.*, vol. 2015, pp. 1–9, 2015.
15. United Nations Economic Commission for Europe (United Nations Economic and Social Council), 'Regulation No 94 — Uniform provisions concerning the approval of vehicles with regard to the protection of the occupants in the event of a frontal collision'. Sep. 20, 2012.
16. Z. Ke, J. Zhang, and M. W. Degner, 'DC Bus Capacitor Discharge of Permanent-Magnet Synchronous Machine Drive Systems for Hybrid Electric Vehicles', *IEEE Trans. Ind. Appl.*, vol. 53, no. 2, pp. 1399–1405, Mar. 2017, https://doi.org/10.1109/TIA.2016.2636279.
17. V. R. Jevremović and B. Jeftenić, 'An Efficient Braking Algorithm for Interior Permanent Magnet Synchronous Motors', Nov. 2005.
18. S. M. Yang and J. Y. Chen, 'Controlled Dynamic Braking for Switched Reluctance Motor Drives With a Rectifier Front End', *IEEE Trans. Ind. Electron.*, vol. 60, no. 11, pp. 4913–4919, Nov. 2013, https://doi.org/10.1109/TIE.2012.2233696.
19. Y. Wang and R. D. Lorenz, 'Creative usage of stator flux linkage to fast brake electric vehicles', in *2016 IEEE Transportation Electrification Conference and Expo (ITEC)*, Jun. 2016, pp. 1–6. https://doi.org/10.1109/ITEC.2016.7520278.
20. G. D. Marques and M. F. Iacchetti, 'Sensorless Frequency and Voltage Control in the Stand-Alone DFIG-DC System', *IEEE Trans. Ind. Electron.*, vol. 64, no. 3, pp. 1949–1957, Mar. 2017, https://doi.org/10.1109/TIE.2016.2624262.
21. T. Guo, J. Liu, S. Vazquez, L. Wu, H. Gao, and L. G. Franquelo, 'Predictive direct power control for grid-connected power converters with an Extended State Observer based dc-link voltage regulator', in *2016 IEEE 25th International Sympo-*

sium on Industrial Electronics (ISIE), Jun. 2016, pp. 1218–1223. https://doi.org/10.1109/ISIE.2016.7745068.

22. B. K. Bose and P. M. Szczesny, 'A microcomputer-based control and simulation of an advanced IPM synchronous machine drive system for electric vehicle propulsion', *IEEE Trans. Ind. Electron.*, vol. 35, no. 4, pp. 547–559, Nov. 1988, https://doi.org/10.1109/41.9178.
23. M. Breznik, V. Ambrožič, and M. Nemec, 'Detection of open circuit fault in battery power supply feeding permanent magnet synchronous motor', *IET Power Electron.*, vol. 11, no. 14, pp. 2377–2384, 2018, https://doi.org/10.1049/iet-pel.2018.5214.
24. H. A. Aebischer and B. Aebischer, 'Improved formulae for the inductance of straight wires', *Adv. Electromagn.*, vol. 3, no. 1, pp. 31–43, 2014.
25. S. K. Kommuri, M. Defoort, H. R. Karimi, and K. C. Veluvolu, 'A Robust Observer-Based Sensor Fault-Tolerant Control for PMSM in Electric Vehicles', *IEEE Trans. Ind. Electron.*, vol. 63, no. 12, pp. 7671–7681, Dec. 2016, https://doi.org/10.1109/TIE.2016.2590993.
26. C.-H. Park, D.-Y. Kim, H.-B. Yeom, Y.-D. Son, and J.-M. Kim, 'A Current Reconstruction Strategy Following the Operation Area in a 1-Shunt Inverter System', *Energies*, vol. 12, no. 8, p. 1423, Jan. 2019, https://doi.org/10.3390/en12081423.
27. S. Skogestad, 'Simple analytic rules for model reduction and PID controller tuning', *J. Process Control*, vol. 13, no. 4, pp. 291–309, Jun. 2003, https://doi.org/10.1016/S0959-1524(02)00062-8.

Arrived: 05. 10. 2021
Accepted: 28. 01. 2022